(Received 23 March 2026, Accepted 12 May 2026, Scheduled 9 June 2026)

Microwave Scattering from a Ship on a Sea Surface: Incoherent Matrix and Coherent Intensity Computed from Single and Double Bouncing PO and MoM-EPILE

Christophe Bourlier[1,*], Prisca Le Dily[2], Nicolas Pinel[3,1], and Romain Bocheux[4]

[1]*IETR (Institut d'Electronique et des Technologies numéRiques) Laboratory, UMR CNRS 6164 Nantes Université, Polytech Nantes, La Chantrerie, Nantes, France*
[2]*IETR and DEMR, ONERA, Université Paris Saclay, Palaiseau, France*
[3]*Icam Ouest, Nantes, France*
[4]*DEMR, ONERA, France*

ABSTRACT: Scattering from a deterministic object in the presence of a randomly rough surface, such as a ship on a sea surface, can be characterized by statistical moments. Full-wave methods, such as the method of moments (MoM), provide accurate results but can be time-consuming. To account for both the gravity and capillary waves, a full sea spectrum is used, which constrains the consideration of a one-dimensional sea surface to include all roughness scales. Asymptotic methods are a good compromise between the computation time and accuracy of the results. In this study, the field scattered by a trapezoidal ship on a 1D sea surface is calculated by iterating the physical optics approximation and incorporating evanescent waves. In addition, the resulting closed-form expressions allow us to derive the associated coherent components analytically by considering a finite and infinite sea surface length. They are validated by comparison to the MoM combined with the extended propagation-inside-layer-expansion (EPILE) method, which can separate bounce orders. The results of the incoherent components, evaluated using a Monte Carlo process, are also shown by introducing a novel concept, based on the centered inter-correlation matrix between the single and double bounces, to quantify the different incoherent contributions. This concept highlights the "backscattering enhancement" phenomenon, only observed for a single rough surface with high slopes.

1. INTRODUCTION

The scattering from a deterministic object in the presence of a randomly rough surface, such as a ship on a sea surface, can be characterized by statistical moments. Firstly, the complex-valued scattered-field measurements with independent realizations of the rough surface are averaged. This leads to the coherent field, or the well-known coherent normalized radar cross section (NRCS), by taking the square modulus. Secondly, the average of the absolute squared scattered field of each realization gives rise to the total NRCS. The incoherent NRCS is obtained by subtracting the coherent NRCS from the total NRCS, corresponding to the centered autocorrelation function of the scattered field.

The well-known four-path model [1–3] approximates the scattered fields into four contributions as shown in Fig. 1: 1) The fields scattered by the sea surface A (ψ_{A}) and object B (ψ_{B}) are assumed to be alone (no coupling). 2) The field scattered by B and then by A (ψ_{BA}). 3) Its reverse way, that is, the field scattered by A and then by B (ψ_{AB}). 4) The field scattered by A, then by B, again by A (ψ_{ABA}) and the reverse path (ψ_{BAB}) is not considered. As shown further in this paper from the method of moments (MoM) [4–6] combined with the extended propagation-inside-layer-expansion (EPILE) [7, 8], for an object near the surface, the fourth path contribution $\psi_{\mathrm{ABA}} + \psi_{\mathrm{BAB}}$ is negligible compared to the contribution of the sum of the lower order paths. It means that the total scattered far field can be approximated by the sum of four contributions, named ψ_{A}, ψ_{B}, ψ_{AB}, and ψ_{BA}. Based on the MoM, EPILE allows us to distinguish the different coupling contributions between two scatterers (here A and B), thanks to a series expansion. The zeroth-order EPILE rigorously calculates the scattered field associated with the single bounce between A and B ($\psi_{\mathrm{BA}} + \psi_{\mathrm{AB}}$), whereas the first-order EPILE rigorously calculates the scattered fields associated with the triple bounces ($\psi_{\mathrm{ABA}} + \psi_{\mathrm{BAB}}$). Similarly, it is also possible to rigorously calculate ψ_{A} and ψ_{B}.

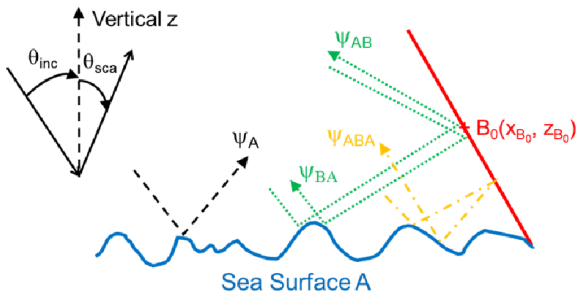

FIGURE 1. Illustration of the fourth path model: Single (black lines), double (green lines) and triple (orange line and ψ_{BAB} is not shown) bounces.

* Corresponding author: Christophe Bourlier (christophe.bourlier@univ-nantes.fr).

The scattered fields ψ_i with $i = \{\mathrm{A}, \mathrm{B}, \mathrm{AB}, \mathrm{BA}\}$ can also be derived from asymptotic theories, such as the Kirchhoff approximation (KA), named physical optics (PO) for a perfectly-conducting scatterer, the KA reduced to the geometrical optics (GO) approximation, and the small slope approximation (SSA) [9]. Recently, for a 3D problem (i.e., 2D-surfaces), Gedney et al. [10] analytically derived the coherent components of ψ_i (as well as ψ_{ABA}). Their formulation is based on Voronovich's works [11] in the sense that the rough surface scattering theory is applied. In addition, the interactions between the rough surface and the object are modeled using a decoupled plane wave approach. This leads to each contribution being related to bounces, such as iterated PO combined with the Weyl decomposition of the Green function, in which the evanescent waves are omitted. Di Simone et al. [12] applied GO to derive incoherent NRCS. The advantages of such methods are that the sea surface is not meshed, avoiding the application of a Monte Carlo (MC) procedure to compute statistical moments. In this study, the PO is also applied with special attention to the inclusion of the evanescent waves in the derivation of ψ_{AB} and ψ_{BA}. For an object far from the surface, this contribution can be neglected as published in [10], but for a ship on a surface, it may contribute. The resulting coherent NRCSs are derived and compared with the full-wave MoM-EPILE to validate them.

Hybrid methods combining asymptotic methods, such as SPM, KA, or Shooting bouncing ray (SBR), and exact methods can be found in [13–19]. They need the generation of a collection of independent rough surfaces to assess the statistical moments. When a gravity wave spectrum is employed, modeled as a Gaussian or sea-like Pierson-Moskowitz or Joint North Sea Wave Project (JONSWAP) spectrum, the surface area (or surface length for a 1D surface) is reduced for numerical purposes. This implies that a part of the large scale roughness is neglected. Moreover, it is well known that away from the specular direction, the capillary waves can contribute to the incoherent NRCS. In this paper, to include both the gravity and capillary waves, the Elfouhaily et al. [20] full sea spectrum model is used. For a wind speed of 6 m/s (fully-developed sea), this implies that the surface length must be of the order of 60 m to include all the roughness scales. For microwave scattering, with a sampling step of ten points per wavelength, the number of surface samples is of the order of ten thousand. This constraint forces us to consider a 1D surface to compute the scattered field from the MoM with a full sea spectrum.

The remainder of this paper is organized as follows. For two perfectly-conducting plates, one of which is rough, and from PO, Section 2 derives the scattered far fields ψ_i for the single and double bounces. Section 3 addresses the calculation of the coherent component using the Weyl decomposition. Section 4 presents numerical results for a trapezoidal ship on a rough sea surface. The different formulations (with and without the contribution of the evanescent waves) of the PO are compared with the MoM-EPILE on a single realization and then, on several surface realizations to calculate the coherent NRCS.

Mathematically, the incoherent NRCS is related to the centered auto-correlation function of the scattered field ψ defined as $\left\langle |\psi|^2 \right\rangle - |\langle \psi \rangle|^2$, where $\left\langle |\psi|^2 \right\rangle = \langle \psi \psi^* \rangle$ is the auto-correlation function of ψ. The symbol $\langle \cdot \rangle$ represents the ensemble average over the random variables on which ψ depends, and * denotes the complex conjugate. As $\psi \approx \psi_{\mathrm{A}} + \psi_{\mathrm{B}} + \psi_{\mathrm{AB}} + \psi_{\mathrm{BA}} = \sum_{i=1}^{4} \psi_i$, where $i = \{\mathrm{A}, \mathrm{B}, \mathrm{AB}, \mathrm{BA}\}$, it is very relevant to calculate the inter-correlation function $c_{ij} = \left\langle \psi_i \psi_j^* \right\rangle$ between different contributions. Similarly, the incoherent NRCS related to c_{ij} is defined as $\sigma_{ij} = \left\langle \psi_i \psi_j^* \right\rangle - \langle \psi_i \rangle \left\langle \psi_j^* \right\rangle$, where σ_{ij} is the centered inter-correlation function between ψ_i and ψ_j. Since the length of i is 4, the incoherence degree among the four contributions to be computed using a square matrix of size 4×4. From a Monte Carlo process, the resulting incoherent NRCS matrix is also evaluated from the PO and compared with the full-wave MoM-EPILE. To the best of our knowledge, this is the first time that such simulations have been published using both the PO asymptotic approach and the full-wave MoM. This study will allow us to quantify the factors that contribute the most in order to calculate them in the future from an analytical approach, similar to the coherent components.

2. DERIVATION OF THE SCATTERED FIELDS

As depicted in Fig. 2, this section addresses the derivation of the scattered field from two plates, one of which is rough. First, the field scattered by an isolated scatterer is derived using the first-order physical optics (PO1) approximation. Next, the coupling between the two objects is accounted for by iterating PO (PO2).

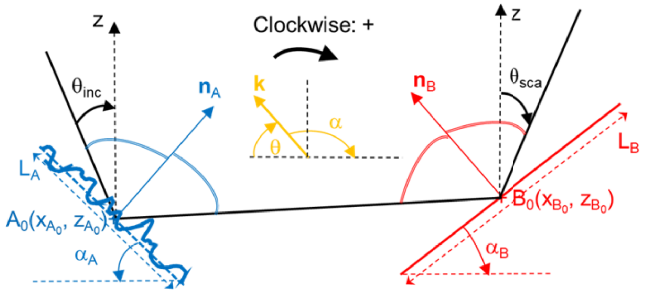

FIGURE 2. Illustration of the scattering problem: Two perfectly-conducting plates, one of which is rough.

2.1. First-Order Physical Optics Approximation

For TE polarization and a perfectly-conducting surface, from PO1, the scattered field at the observation point $\boldsymbol{r}'$ is expressed as [5]

$$\psi_{\mathrm{sca}}(\boldsymbol{r}') = -2 \int_S g(\boldsymbol{r}, \boldsymbol{r}') \frac{\partial \psi_{\mathrm{inc}}(\boldsymbol{r})}{\partial n} dS, \tag{1}$$

where ψ_{inc} is the incident field illuminating the scatterer, g the two-dimensional scalar Green function, S the object surface of coordinates $\boldsymbol{r} = (x, z(x))$ and $\partial f / \partial n = \boldsymbol{\nabla} f \cdot \hat{\boldsymbol{n}}$, where $\hat{\boldsymbol{n}}$ is a normal to the surface, and $\boldsymbol{\nabla} = \partial/\partial x \hat{\boldsymbol{x}} + \partial/\partial z \hat{\boldsymbol{z}}$ is the gradient operator. The function g is defined as

$$g(\boldsymbol{r}, \boldsymbol{r}') = \frac{j}{4} \mathrm{H}_0^{(1)}(k_0 \|\boldsymbol{r}' - \boldsymbol{r}\|), \tag{2}$$

where k_0 is the wavenumber in free space and $\mathrm{H}_0^{(1)}$ the Hankel function of the first kind and zeroth order.

For TM polarization and a perfectly-conducting surface, from PO1, the scattered field at the observation point $\boldsymbol{r}'$ is expressed as

$$\psi_{\text{sca}}(\boldsymbol{r}') = 2\int_S \psi_{\text{inc}}(\boldsymbol{r})\frac{\partial g(\boldsymbol{r},\boldsymbol{r}')}{\partial n}dS. \tag{3}$$

2.2. Second-Order Physical Optics Approximation (PO2)

The field scattered by plate A, $\psi_{\text{sca,A}}(\boldsymbol{r})$, can interact with that of B. To derive the corresponding scattered field, the PO1 approximation is iterated. For TE polarization, from Eq. (1), this leads to

$$\begin{aligned}\psi_{\text{sca,AB}}(\boldsymbol{r}') &= -2\int_{S_B} g(\boldsymbol{r}_B,\boldsymbol{r}')\frac{\partial\psi_{\text{sca,A}}(\boldsymbol{r}_B)}{\partial n_B}dS_B\\ &= 4\int_{S_A}\int_{S_B} g(\boldsymbol{r}_B,\boldsymbol{r}')\frac{\partial}{\partial n_B}\left[g(\boldsymbol{r}_A,\boldsymbol{r}_B)\frac{\partial\psi_{\text{inc}}(\boldsymbol{r}_A)}{\partial n_A}\right]dS_AdS_B\\ &= 4\int_{S_A}\int_{S_B} g(\boldsymbol{r}_B,\boldsymbol{r}')\frac{\partial\psi_{\text{inc}}(\boldsymbol{r}_A)}{\partial n_A}\frac{\partial g(\boldsymbol{r}_A,\boldsymbol{r}_B)}{\partial n_B}dS_AdS_B. \end{aligned}\tag{4}$$

For the TM polarization, the use of Eq. (3) leads to

$$\begin{aligned}\psi_{\text{sca,AB}}(\boldsymbol{r}') &= 2\int_{S_B}\psi_{\text{sca,A}}(\boldsymbol{r}_B)\frac{\partial g(\boldsymbol{r}_B,\boldsymbol{r}')}{\partial n_B}dS_B\\ &= 4\int_{S_A}\int_{S_B}\psi_{\text{inc}}(\boldsymbol{r}_A)\frac{\partial g(\boldsymbol{r}_A,\boldsymbol{r}_B)}{\partial n_A}\frac{\partial g(\boldsymbol{r}_B,\boldsymbol{r}')}{\partial n_B}dS_AdS_B. \end{aligned}\tag{5}$$

The normal derivative of g is expressed as

$$\frac{\partial g(\boldsymbol{r}_A,\boldsymbol{r}_B)}{\partial n_{A,B}} = \pm\frac{jk_0}{4}H_{A,B}(\boldsymbol{r}_A,\boldsymbol{r}_B), \tag{6}$$

where

$$H_{A,B} = \frac{\mathrm{H}_1^{(1)}(k_0r_{AB})\left[-(x_B-x_A)\gamma_{A,B}+z_B-z_A\right]}{r_{AB}}, \tag{7}$$

and $\boldsymbol{r}_A=(x_A,z_A)$, $\boldsymbol{r}_B=(x_B,z_B)$, $\gamma_A=z'_A$, $\gamma_B=z'_B$ and

$$r_{AB} = \|\boldsymbol{r}_A-\boldsymbol{r}_B\| = \sqrt{(x_A-x_B)^2+(z_A-z_B)^2}. \tag{8}$$

2.3. Observation in Far Field and for a Plane Incident Wave

If the receiver is located in the far field, then

$$g(\boldsymbol{r}_B,\boldsymbol{r}') \approx Aje^{-j\boldsymbol{k}_{\text{sca}}\cdot\boldsymbol{r}_B} \text{ where } A=\sqrt{\frac{1}{8\pi k_0r'}}e^{j(k_0r'-\pi/4)}, \tag{9}$$

and

$$\frac{\partial g(\boldsymbol{r}_B,\boldsymbol{r}')}{\partial n_B} \approx Ae^{-j\boldsymbol{k}_{\text{sca}}\cdot\boldsymbol{r}_B}(\boldsymbol{k}_{\text{sca}}\cdot\hat{\boldsymbol{n}}_B), \tag{10}$$

where $\boldsymbol{k}_{\text{sca}} = k_0(\sin\theta_{\text{sca}},\cos\theta_{\text{sca}})$ is the direction of the receiver, in which θ_{sca} is the scattering angle defined from the vertical direction z, as shown in Fig. 1. k_0 is the wavenumber in free space. In addition, for an incident wave assumed to be plane, $\psi_{\text{inc}}(\boldsymbol{r}) = e^{j\boldsymbol{k}_{\text{inc}}\cdot\boldsymbol{r}}$, we have

$$\frac{\partial\psi_{\text{inc}}(\boldsymbol{r})}{\partial n} = j(\boldsymbol{k}_{\text{inc}}\cdot\hat{\boldsymbol{n}})\psi_{\text{inc}}(\boldsymbol{r}) = j(\boldsymbol{k}_{\text{inc}}\cdot\hat{\boldsymbol{n}})e^{j\boldsymbol{k}_{\text{inc}}\cdot\boldsymbol{r}}, \tag{11}$$

where $\boldsymbol{k}_{\text{inc}} = k_0(\sin\theta_{\text{inc}},-\cos\theta_{\text{inc}})$ is the direction of the transmitter, where θ_{inc} is the incident angle defined from the vertical direction z, as shown in Fig. 1.

Substituting Eqs. (9), (10), and (11) into Eqs. (1) and (3), for the TE and TM polarizations and from the PO1 approximation, we obtain in the far field

$$\psi^{\infty}_{\text{sca}}(\boldsymbol{r}') = 2A\int_S(\boldsymbol{k}_{\text{inc}}\cdot\hat{\boldsymbol{n}})e^{j(\boldsymbol{k}_{\text{inc}}-\boldsymbol{k}_{\text{sca}})\cdot\boldsymbol{r}}dS \text{ (TE)}, \tag{12}$$

and

$$\psi^{\infty}_{\text{sca}}(\boldsymbol{r}') = 2A\int_S(\boldsymbol{k}_{\text{sca}}\cdot\hat{\boldsymbol{n}})e^{j(\boldsymbol{k}_{\text{inc}}-\boldsymbol{k}_{\text{sca}})\cdot\boldsymbol{r}}dS \text{ (TM)}, \tag{13}$$

respectively, where $\boldsymbol{r}=\{\boldsymbol{r}_A,\boldsymbol{r}_B\}$ and $S=\{S_A,S_B\}$.

Substituting Eqs. (9), (10) and (11) into Eq. (4), for TE polarization and from the PO2 approximation, we obtain in the far field

$$\begin{aligned}\psi^{\infty}_{\text{sca,AB}}(\boldsymbol{r}') &= Ak_0\int_{S_A}\int_{S_B}\frac{\partial\psi_{\text{inc}}(\boldsymbol{r}_A)}{\partial n_A}e^{-j\boldsymbol{k}_{\text{sca}}\cdot\boldsymbol{r}_B}H_BdS_AdS_B\\ &= Ajk_0\int_{S_A}\int_{S_B}e^{j\boldsymbol{k}_{\text{inc}}\cdot\boldsymbol{r}_A-j\boldsymbol{k}_{\text{sca}}\cdot\boldsymbol{r}_B}(\boldsymbol{k}_{\text{inc}}\cdot\hat{\boldsymbol{n}}_A)\\ &\quad H_BdS_AdS_B. \end{aligned}\tag{14}$$

Substituting Eqs. (9) and (10) into Eq. (5), for TM polarization, we obtain in the far field

$$\begin{aligned}\psi^{\infty}_{\text{sca,AB}}(\boldsymbol{r}') &= 2\int_{S_B}\psi_{\text{inc}}(\boldsymbol{r}_B)\frac{\partial g(\boldsymbol{r}_B,\boldsymbol{r}')}{\partial n_B}dS_B\\ &= Ajk_0\int_{S_A}\int_{S_B}e^{j\boldsymbol{k}_{\text{inc}}\cdot\boldsymbol{r}_A-j\boldsymbol{k}_{\text{sca}}\cdot\boldsymbol{r}_B}(\boldsymbol{k}_{\text{sca}}\cdot\hat{\boldsymbol{n}}_B)\\ &\quad H_AdS_AdS_B. \end{aligned}\tag{15}$$

The field scattered by B and propagating from B to A is obtained from ψ_{AB} by changing $(\boldsymbol{r}_A,\boldsymbol{r}_B,\boldsymbol{k})$ to $(\boldsymbol{r}_B,\boldsymbol{r}_A,-\boldsymbol{k})$. This leads to

$$\psi^{\infty}_{\text{sca,BA}}(\boldsymbol{r}') = \begin{cases}\text{Eq. (14)}|_{(\boldsymbol{r}_A,\boldsymbol{r}_B,\boldsymbol{k})\to(\boldsymbol{r}_B,\boldsymbol{r}_A,-\boldsymbol{k})} & \text{TE}\\ \text{Eq. (15)}|_{(\boldsymbol{r}_A,\boldsymbol{r}_B,\boldsymbol{k})\to(\boldsymbol{r}_B,\boldsymbol{r}_A,-\boldsymbol{k})} & \text{TM}\end{cases}, \tag{16}$$

2.4. Weyl's Representation

The Weyl representation was applied to derive a closed-form expression for the NRCS. This decomposition allows us to express the Green function as the sum of plane waves, which are both evanescent and propagative. It writes

$$g(\boldsymbol{r}_A,\boldsymbol{r}_B) = \frac{j}{4\pi}\int_{-\infty}^{+\infty}\frac{e^{j(x_A-x_B)k_x+j|z_A-z_B|k_z}dk_x}{k_z}, \tag{17}$$

where $k_x^2 + k_z^2 = k_0^2$. Letting $k_x = -k_0 \cos\theta$, $k_z = k_0 \sin\theta$, $dk_x/k_z = k_0 \sin\theta d\theta / k_z = d\theta$ and one has

$$g\left(\boldsymbol{r}_A, \boldsymbol{r}_B\right) = \frac{j}{4\pi} \int_{C_{z,\theta}} e^{jk_0[(x_B - x_A)\cos\theta + |z_A - z_B|\sin\theta]} d\theta, \quad (18)$$

where $C_{z,\theta}$ is the integration contour in the complex plane over θ. If the evanescent waves are omitted, that is, if $\theta \in \mathbb{R}$, we can show that

$$g\left(\boldsymbol{r}_A, \boldsymbol{r}_B\right) \approx \frac{j}{4\pi} \int_{\theta} e^{j\boldsymbol{k}\cdot(\boldsymbol{r}_B - \boldsymbol{r}_A)} d\theta, \quad (19)$$

where $\boldsymbol{k} = k_0(-\cos\theta, \sin\theta) = k_0(\cos\alpha, \sin\alpha)$, in which $\theta \in [0;\pi]$, $\alpha = \pi - \theta$ and $\alpha \in [0;\pi]$ because we assume that $z_B \geq z_A$ (object is above the sea surface). In addition

$$\frac{\partial g\left(\boldsymbol{r}_A, \boldsymbol{r}_B\right)}{\partial n_{A,B}} = \pm \frac{1}{4\pi} \int_{\alpha} e^{j\boldsymbol{k}\cdot(\boldsymbol{r}_B - \boldsymbol{r}_A)} \left(\hat{\boldsymbol{n}}_{A,B} \cdot \boldsymbol{k}\right) d\alpha. \quad (20)$$

Comparing with Eq. (6), we obtain

$$H_{A,B} = \frac{1}{jk_0\pi} \int_{\alpha} e^{j\boldsymbol{k}\cdot(\boldsymbol{r}_B - \boldsymbol{r}_A)} \left(\hat{\boldsymbol{n}}_{A,B} \cdot \boldsymbol{k}\right) d\alpha. \quad (21)$$

2.5. Scattered Fields in Far Zone

For two smooth plates, we can write for $i = \{\mathrm{A}, \mathrm{B}\}$

$$z_i\left(x_i\right) = z_{i_0} + \gamma_{i_0}\left(x_i - x_{i_0}\right), \quad (22)$$

where $(x_{i_0} z_{i_0})$ is the i plate center and γ_{i_0} its slope, which is constant. For any vector $\boldsymbol{w} = (w_x, w_z)$, one has

$$\begin{aligned} \boldsymbol{r}_i \cdot \boldsymbol{w} &= x_i w_x + \left[z_{i_0} + \gamma_{i_0}\left(x_i - x_{i_0}\right)\right] w_z \\ &= u_i\left(w_x + \gamma_{i_0} w_z\right) + x_{i_0} w_x + z_{i_0} w_z \\ &= u_i\left(w_x + \gamma_{i_0} w_z\right) + \boldsymbol{r}_{i_0} \cdot \boldsymbol{w}, \end{aligned} \quad (23)$$

where $u_i = x_i - x_{i_0}$ and $\boldsymbol{r}_{i_0} = (x_{i_0}, z_{i_0})$. Plate A is now considered rough, and its profile is assumed to be

$$\eta\left(x_A\right) = z_A\left(x_A\right) + \xi\left(x_A\right), \quad (24)$$

where ξ is a random variable with a zero mean value $\langle \xi \rangle = 0$ and a surface height variance $\langle \xi^2 \rangle = \sigma_\xi^2$. In addition, the slope $\partial\eta/\partial x_A = \gamma_{A_0} + \gamma$, where $\gamma = \partial\xi/\partial x_A$.

Using PO1 in the far field, from Eqs. (12) and (13), the scattered field is written as

$$\psi_A = A_1 \int_{-l_A^-}^{+l_A^+} \left(\boldsymbol{k}_P \cdot \boldsymbol{n}_A\right) e^{ju(w_x + \gamma_{A_0} w_z) + j\xi(u) w_z} du, \quad (25)$$

$$\psi_B = 2A\left(\boldsymbol{k}_P \cdot \boldsymbol{n}_B\right) e^{j\boldsymbol{r}_{B_0}\cdot\boldsymbol{w}} F\left(w_x + \gamma_{B_0} w_z, l_B^+, l_B^-\right), \quad (26)$$

where $\psi_{\mathrm{A,B}} = \psi^{\infty}_{\mathrm{sca,A,B}}\left(\boldsymbol{r}'\right)$ and

$$F\left(w, l^+, l^-\right) = \left(l^+ + l^-\right) e^{\frac{jw(l^+ - l^-)}{2}} \mathrm{sinc}\left(\frac{w(l^+ + l^-)}{2}\right), \quad (27)$$

$$\begin{cases} A_1 = 2Ae^{j\boldsymbol{r}_{A_0}\cdot\boldsymbol{w}} = \frac{j}{2}\sqrt{\frac{2}{\pi k_0 r'}} e^{j(k_0 r' - \pi/4)} e^{j\boldsymbol{r}_{A_0}\cdot\boldsymbol{w}} \\ \boldsymbol{w} = \boldsymbol{k}_{\mathrm{inc}} - \boldsymbol{k}_{\mathrm{sca}}, \boldsymbol{n}_i = -\gamma_i \hat{\boldsymbol{x}} + \hat{\boldsymbol{z}}, l_i^{\pm} = L_i^{\pm} \left|\cos\alpha_i\right| \\ \mathrm{TE}: P = \mathrm{inc}, \mathrm{TM}: P = \mathrm{sca} \end{cases}, \quad (28)$$

where α_i is the plate inclination angle in the $\hat{\boldsymbol{x}}$ direction. If no shadow occurs, the surface is entirely illuminated and $L_i^+ = L_i^- = L_i/2$, where L_i is the surface length, $u_i \in [-l_i; l_i]$ and $F\left(w, l, l\right) = L\mathrm{sinc}(wL/2)$, where $L = 2l$. Otherwise, $u_i \in [-l_i^-; l_i^+]$, where $l_i^- > 0$ and $0 < l_i^{\pm} \leq l_i/2$.

In the far field, substituting Eq. (21) into Eqs. (14) and (15), we show that

$$\begin{aligned} \psi_{\mathrm{AB}}\left(\boldsymbol{r}'\right) &= \frac{A}{\pi} \int_{x_A} \int_{x_B} \int_{\alpha} e^{j\boldsymbol{k}_1\cdot\boldsymbol{r}_A + j\boldsymbol{k}_2\cdot\boldsymbol{r}_B} \left(\boldsymbol{k}_A \cdot \boldsymbol{n}_A\right) \\ &\quad \times \left(\boldsymbol{k}_B \cdot \boldsymbol{n}_B\right) d\alpha dx_B dx_A, \end{aligned} \quad (29)$$

where $dS_{A,B}\hat{\boldsymbol{n}}_{A,B} = dx_{A,B}\boldsymbol{n}_{A,B}$ and $\hat{\boldsymbol{n}}_{A,B} = \boldsymbol{n}_{A,B}\sqrt{1 + \gamma_{A,B}^2}$. In addition

$$\begin{cases} \boldsymbol{k}_1 = \boldsymbol{k}_{\mathrm{inc}} - \boldsymbol{k}, \boldsymbol{k}_2 = \boldsymbol{k} - \boldsymbol{k}_{\mathrm{sca}} \\ \mathrm{TE}: \boldsymbol{k}_A = \boldsymbol{k}_{\mathrm{inc}}, \boldsymbol{k}_B = \boldsymbol{k} \\ \mathrm{TM}: \boldsymbol{k}_A = \boldsymbol{k}, \boldsymbol{k}_B = \boldsymbol{k}_{\mathrm{sca}} \end{cases}. \quad (30)$$

The field scattered by B and propagating from B to A is obtained from ψ_{AB} by changing $(\boldsymbol{r}_A, \boldsymbol{r}_B, \boldsymbol{k})$ to $(\boldsymbol{r}_B, \boldsymbol{r}_A, -\boldsymbol{k})$. This leads to

$$\begin{aligned} \psi_{\mathrm{BA}}\left(\boldsymbol{r}'\right) &= \frac{A}{\pi} \int_{x_A} \int_{x_B} \int_{\alpha} e^{j\boldsymbol{K}_1\cdot\boldsymbol{r}_A + j\boldsymbol{K}_2\cdot\boldsymbol{r}_B} \left(\boldsymbol{K}_A \cdot \boldsymbol{n}_A\right) \\ &\quad \times \left(\boldsymbol{K}_B \cdot \boldsymbol{n}_B\right) d\alpha dx_B dx_A, \end{aligned} \quad (31)$$

where

$$\begin{cases} \boldsymbol{K}_1 = -\boldsymbol{k}_{\mathrm{sca}} - \boldsymbol{k}, \boldsymbol{K}_2 = \boldsymbol{k} + \boldsymbol{k}_{\mathrm{inc}} \\ \mathrm{TE}: \boldsymbol{K}_A = -\boldsymbol{k}, \boldsymbol{K}_B = \boldsymbol{k}_{\mathrm{inc}} \\ \mathrm{TM}: \boldsymbol{K}_A = \boldsymbol{k}_{\mathrm{sca}}, \boldsymbol{K}_B = -\boldsymbol{k} \end{cases}. \quad (32)$$

It is important to underline that

$$\begin{aligned} e^{j\boldsymbol{k}_1\cdot\boldsymbol{r}_A}\left(\boldsymbol{k}_A \cdot \boldsymbol{n}_A\right) &= e^{jk_{1,x}x_A + jk_{1,z}[z_A + \gamma_A(x_A - x_{A_0})]} \\ &\quad \times \left[-k_{A,x}\left(\gamma + \gamma_{A_0}\right) + k_{A,z}\right] e^{jk_{1,z}\xi}, \end{aligned} \quad (33)$$

where the second line is a random function, because of γ and ξ.

3. COHERENT COMPONENT

The coherent component is defined as

$$\mathrm{Coh} = \langle \psi \rangle = \sum_{i=1}^{i=4} \langle \psi_i \rangle, \quad (34)$$

where $i = \{\mathrm{A}, \mathrm{B}, \mathrm{AB}, \mathrm{BA}\}$ and $\langle \cdot \rangle$ is the ensemble average operator on all random variables.

3.1. Component $\langle\psi_{\mathrm{A}}\rangle$

From Eq. (25), one has

$$\langle\psi_{\mathrm{A}}\rangle = A_1 \int_{-l_A^-}^{+l_A^+} e^{ju(w_x+\gamma_{A_0}w_z)} \times \left\langle \left[-k_{P,x}\left(\gamma+\gamma_{A_0}\right)+k_{P,z}\right] e^{j\xi w_z}\right\rangle du. \quad (35)$$

For a Gaussian stationary process, $\left\langle e^{j\xi w_z}\right\rangle = e^{-w_z^2\sigma_\xi^2/2}$ and

$$\left\langle \gamma e^{j\xi w_z}\right\rangle = \frac{1}{jw_z}\frac{\partial}{\partial x}\left\langle e^{j\xi(x) w_z}\right\rangle = 0, \quad (36)$$

because $\left\langle e^{j\xi w_z}\right\rangle$ is independent of x. This implies that the expected values are independent of u, and the integration over u leads to

$$\langle\psi_{\mathrm{A}}\rangle = e^{-(\cos\theta_{\mathrm{inc}}+\cos\theta_{\mathrm{sca}})^2 k_0^2\sigma_\xi^2/2}\psi_{\mathrm{A},0}, \quad (37)$$

where $\psi_{\mathrm{A},0}$ is the field scattered by the smooth plate A expressed as

$$\psi_{\mathrm{A},0} = 2A\left(\boldsymbol{k}_P\cdot\boldsymbol{n}_{A_0}\right) e^{j\boldsymbol{r}_{A_0}\cdot\boldsymbol{w}} F\left(w_x+\gamma_{A_0}w_z, l_A^+, l_A^-\right), \quad (38)$$

where F is given by Eq. (27). From Eq. (28), $w_z = \boldsymbol{w}\cdot\hat{\boldsymbol{z}} = -k_0(\cos\theta_{\mathrm{inc}}+\cos\theta_{\mathrm{sca}})$. Thus, as the ratio σ_ξ/λ_0 or/and $(\theta_{\mathrm{inc}},\theta_{\mathrm{sca}})$ increases, the Rayleigh roughness parameter $w_z^2\sigma_\xi^2$ increases, and the coherent contribution decreases. In addition, $|F|$ is maximum when $w_x+\gamma_{A_0}w_z = 0$, leading to $\gamma_{A_0} = -w_x/w_z = \tan([\theta_{\mathrm{inc}}-\theta_{\mathrm{sca}}]/2)$. If the plate is horizontal, then $\gamma_{A_0} = 0$, and as expected, the maximum occurs for $\theta_{\mathrm{inc}} = \theta_{\mathrm{sca}}$, corresponding to the specular direction.

If $l_A^+ + l_A^- \to \infty$, $\psi_{\mathrm{A},0}$ is expressed in Eq. (A4).

3.2. Component $\langle\psi_{\mathrm{B}}\rangle$

Because plate B is smooth, the scattered field is deterministic. This implies that

$$\langle\psi_{\mathrm{B}}\rangle = \psi_{\mathrm{B}} = \text{Eq. (26)}. \quad (39)$$

3.3. Components $\langle\psi_{\mathrm{AB}}\rangle$ and $\langle\psi_{\mathrm{BA}}\rangle$

From Eqs. (29) and (33), $\langle\psi_{AB}(\boldsymbol{r}')\rangle$ needs to derive

$$\begin{aligned}\left\langle e^{j\boldsymbol{k}_1\cdot\boldsymbol{r}_A}\left(\boldsymbol{k}_A\cdot\boldsymbol{n}_A\right)\right\rangle &= e^{jk_{1,x}x_A+jk_{1,z}[z_A+\gamma_{A_0}(x_A-x_{A_0})]} \\ &\times\left\langle\left[-k_{A,x}\left(\gamma+\gamma_{A_0}\right)+k_{A,z}\right] e^{jk_{1,z}\xi}\right\rangle \\ &= e^{jk_{1,x}x_A+jk_{1,z}[z_A+\gamma_{A_0}(x_A-x_{A_0})]} \\ &\times\left(-k_{A,x}\gamma_{A_0}+k_{A,z}\right) e^{-\sigma_\xi^2 k_{1,z}^2/2}. \quad (40)\end{aligned}$$

Substituting the above equation into Eq. (29) and integrating over x_A and x_B, we show for Gaussian statistics that

$$\begin{aligned}\langle\psi_{\mathrm{AB}}\rangle &= \frac{Al_Al_B}{\pi}\int_\alpha \left(\boldsymbol{k}_A\cdot\boldsymbol{n}_{A_0}\right)\left(\boldsymbol{k}_B\cdot\boldsymbol{n}_B\right) e^{j\boldsymbol{r}_{A_0}\cdot\boldsymbol{k}_1+j\boldsymbol{r}_{B_0}\cdot\boldsymbol{k}_2} \\ &\times e^{-\sigma_\xi^2 k_{1,z}^2/2} F\left(k_{1,x}+\gamma_{A_0}k_{1,z}, l_A^+, l_A^-\right) \\ &\times F\left(k_{2,x}+\gamma_{B_0}k_{2,z}, l_B^+, l_B^-\right) d\alpha, \quad (41)\end{aligned}$$

and

$$\langle\psi_{\mathrm{BA}}\rangle = \langle\psi_{\mathrm{AB}}\rangle|_{\boldsymbol{k}_{1,2,A,B}\to\boldsymbol{K}_{1,2,A,B}}. \quad (42)$$

If $l_A^+ + l_A^- \to \infty$, $\langle\psi_{\mathrm{AB}}\rangle$ and $\langle\psi_{\mathrm{BA}}\rangle$ are expressed by Eqs. (A8) and (A12), where the integration over α is suppressed.

4. NUMERICAL RESULTS

4.1. Choice of the Surface Length

The upper surface length (i.e., large-scale roughness) L_1 is related to the lower wave number $k_1 = \pi/L_1$ (a bilateral spectrum is used to generate the surface) of the sea surface height spectrum S for which S is negligible. Typically, for the Elfouhaily et al. spectrum, $k_1 \approx 0.3k_p$, where $k_p \approx 0.84^2\times 9.81/u_{10}^2 \approx 6.92/u_{10}^2$ for a fully developed sea, and k_p equals the wavenumber of the most energetic sea wave (largest height). For $u_{10} = \{3,6\}$ m/s, $k_p \approx \{0.769, 0.192\}$ rad/m and $L_1 \approx \{13.6, 54.5\}$ m. So, taking a scene length $L_{\mathrm{sur}} = 80$ m (Fig. 3) is a good choice to capture the large-scale roughness.

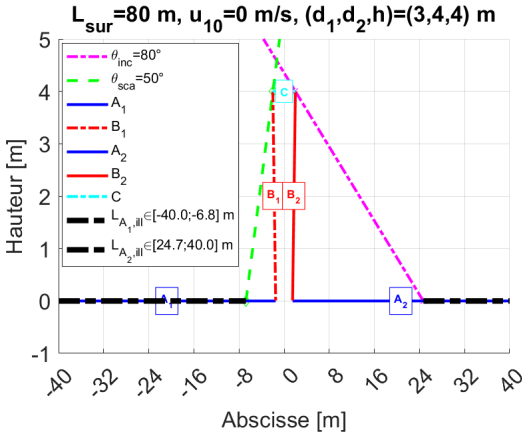

FIGURE 3. Illustration of the geometry. The sea surface $\mathrm{A} = \mathrm{A}_1 \cup \mathrm{A}_2$ is smooth.

The spatial sampling step $\Delta x = \lambda_0/n$, where $n = 10$, and λ_0 is the radar wavelength, which is sufficient for a sea surface because the slope standard deviation does not exceed 0.2 in the numerical results. More precisely, in addition to λ_0, Δx can also depend on the facet inclination, where n becomes $n\sqrt{1+\langle z'^2\rangle}$, and z' is the surface slope. For a linear sea surface (without breaking waves), $\langle z'^2\rangle < 0.1 \ll 1$.

4.2. Smooth Sea Surface

The geometry is shown in Fig. 3. The boat has a trapezoidal shape and is composed of three smooth plates B_1 (left hull), C (top plate), and B_2 (right hull). In the title, d_2 is the C plate length and d_1 the horizontal distance between the bottoms of the right and left hulls. Therefore, the hull has an angle of inclination defined from x equal to $\alpha_B = -\arctan(h/[2(d_2-d_1)]) \approx -82.9°$. The scene is split into five sub-geometries A_1 (left sea surface), A_2 (right sea surface), B_1, B_2, and C. The sea surface is perfectly flat (wind speed defined at ten meters above the sea mean level $u_{10} = 0$ m/s).

To attenuate the edge diffraction by the surface, the Thorsos [21] tapered incident wave is applied with $g = L_{\mathrm{sur}}/6$ (g controls the extent of the incident wave). The function F is expressed by Eq. (27) and valid for a plane incident wave, and it is replaced by Eq. (B3) to account for the tapered behavior of the Thorsos wave. The incidence and scattering angles are denoted as $\theta_{\mathrm{inc}} \in [0; 80]°$ and $\theta_{\mathrm{sca}} \in [-90; 90]°$, respectively. It is

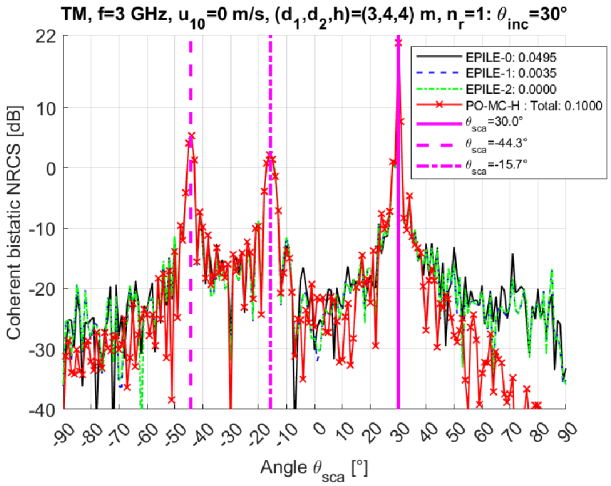

FIGURE 4. Bistatic NRCS in dB scale versus the scattering angle θ_{sca} for $\theta_{\text{inc}} = 30°$. The scene is shown in Fig. 3.

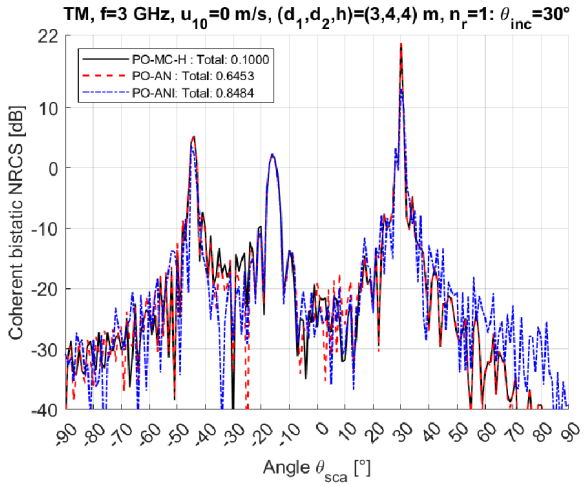

FIGURE 5. Same variations as in Fig. 4.

important to note that the Thorsos wave is not valid at grazing incidence angles. The frequency is $f = 3\,\text{GHz}$, corresponding to a number of unknowns for the MoM $N = 8,906$.

To be consistent with the PO, the shadowing phenomenon must be considered according to the sub-geometry. For instance, as shown in Fig. 3, no shadow occurs for plate C. For A_1, because of the boat, hiding can occur in the transmitter if $\theta_{\text{inc}} < \pi/2 - |\alpha_B|$ ($\theta_{\text{inc}} \geq 0$ and $\alpha_B \in [-\pi/2; 0]$), and masking occurs from the receiver as illustrated by the dashed green line for $\theta_{\text{sca}} = 50°$. Thus, as shown in Fig. 3 (black dashed line), the illuminated surface length $L_{A_1,\text{ill}} < L_{A_1} = (L_{\text{sur}} - d_1)/2 = 38.5$ m is reduced. This length must be considered in Eq. (27), where $l^+ = l_A^+ = L_{A_1,\text{ill}}/2 - x_{A_0}$ and $l^- = l_A^- = L_{\text{sur}}/2 - x_{A_0}$. The same phenomenon must be accounted for plate A_2 (see pink dashed line for $\theta_{\text{inc}} = 80°$). Similarly, plate B_1 is illuminated if $\theta_{\text{inc}} < \pi/2 - |\alpha_B|$, and plate B_2 is never illuminated by the transmitter, meaning that its PO1 contribution vanishes.

The normalized radar cross section (NRCS, dimensionless) is defined as

$$\text{NRCS} = \lim_{r' \to \infty} \frac{r'}{2\eta_0} \frac{|\psi|^2}{p_{\text{inc}}}, \tag{43}$$

where η_0 is the vacuum wave impedance, and p_{inc} is the incident power defined on the rough surface mean plane $z = 0$ (Eq. (1.34) of [5] and behaves as $1/\eta_0$) and ψ (behaves as $1/\sqrt{r'}$, see A_1 in Eq. (28)) scattered far field. The MoM is calculated by radiating the surface currents using the Huygens principle.

We define the geometries $\text{A} = \text{A}_1 \cup \text{A}_2$ and $\text{B} = \text{B}_1 \cup \text{B}_2$. For PO1, this implies that $\psi_{\text{A}} = \psi_{\text{A}_1} + \psi_{\text{A}_2}$ and $\psi_{\text{B}} = \psi_{\text{B}_1} + \psi_{\text{B}_2} = \psi_{\text{B}_1}$ ($\theta_{\text{inc}} \geq 0$). In addition, the ψ_{C} contribution is added. For PO2, $\psi_{\text{AB}} = \psi_{\text{A}_1\text{B}_1} + \psi_{\text{A}_2\text{B}_2}$ and $\psi_{\text{BA}} = \psi_{\text{B}_1\text{A}_1} + \psi_{\text{B}_2\text{A}_2}$. Fig. 3 shows that $\text{A}_1 \cup \text{B}_1$ does not interact with $\text{A}_2 \cup \text{B}_2$ and reversely, and C does not interact with either $\text{A}_1 \cup \text{B}_1$ or $\text{A}_2 \cup \text{B}_2$. The total scattered field is equal to $\psi = \psi_{\text{C}} + \psi_{\text{A}} + \psi_{\text{B}} + \psi_{\text{AB}} + \psi_{\text{BA}}$.

Figures 4 and 5 plot the bistatic NRCS versus the scattering angle θ_{sca} for $\theta_{\text{inc}} = 30°$. The scene is illustrated in Fig. 3. In the legend, the labels mean:

- EPILE-0 [5]: NRCS computed from EPILE only at the zeroth order, allowing us to calculate ψ, which was previously defined and computed from the MoM.
- EPILE-1: NRCS computed from EPILE up to the first order, where the first order was added. This corresponds to the additional contributions ψ_{ABA}, ψ_{BAB} and the potential coupling with plate C.
- EPILE-2: NRCS computed from EPILE up to the second order, where the contributions at the first and second orders are included.
- PO-MC-H: NRCS computed under the PO, by computing ψ using Eqs. (25), (26), (14), or (15) and (16)), where the scattered fields ψ_{AB} and ψ_{BA} are determined without applying the Weyl decomposition. In other words, both the propagative and evanescent waves are included.
- PO-AN: NRCS computed under the PO, by computing ψ, where the scattered fields ψ_{AB} and ψ_{BA} (Eqs. (41) and (42)) are determined by applying the Weyl decomposition and including only the propagative waves.
- PO-ANI: Same as PO-AN, but surfaces A_1 and A_2 are assumed to be of infinite lengths (Eqs. (A8) and (A12)).

In Eqs. (29) and (31), using Eq. (27), the integration over x_B is performed analytically, and two fold-numerical integrations over (x_A, α) are performed.

In the legend, the number corresponds to the relative residual error defined as

$$\text{RRE} = \frac{\text{norm}\left(\text{NRCS}_{\text{Meth}} - \text{NRCS}_{\text{MoM}}\right)}{\text{norm}(\text{NRCS}_{\text{MoM}})}. \tag{44}$$

The NRCS computed from the MoM includes all contributions. It is similar to applying EPILE up to infinity order. EPILE allows us to appreciate the levels of the different contributions associated with the multiple reflections between the boat ($\text{B}_1 \cup \text{C} \cup \text{B}_2$) and the sea ($\text{A}_1 \cup \text{A}_2$).

For all simulations (not shown here), EPILE-3 perfectly matched EPILE-2, and both EPILE-3 and EPILE-2 perfectly

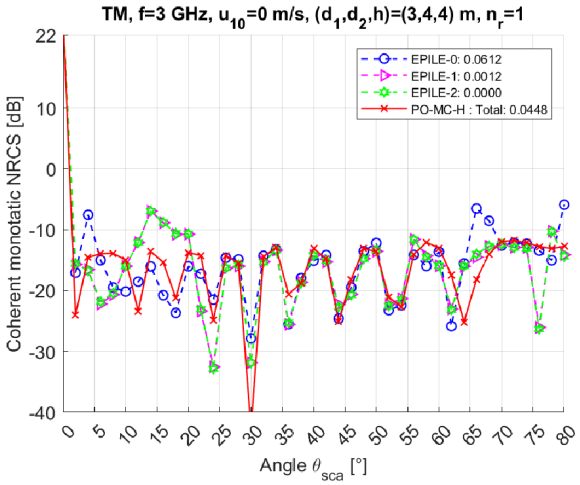

FIGURE 6. Monostatic NRCS in dB scale versus the scattering angle $\theta_{\text{sca}} = -\theta_{\text{inc}}$. The scene is shown in Fig. 3.

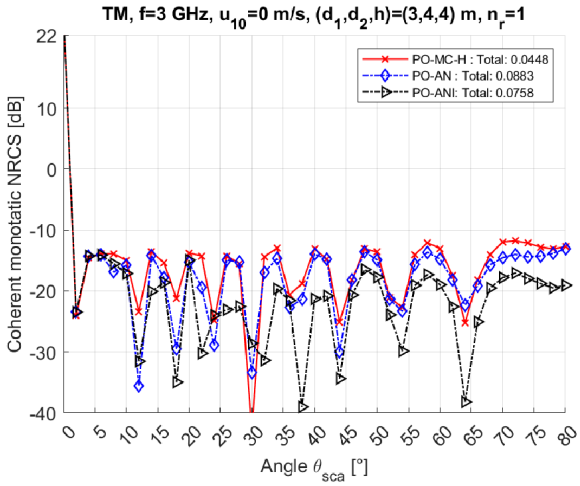

FIGURE 7. Same variations as in Fig. 6.

agreed with the MoM. It means that EPILE-2 can be considered a reference solution.

Figure 4 clearly shows that EPILE converges at the first order, and the difference between EPILE-0 and EPILE-1 is slight. It explains why PO predicts good results compared to EPILE-2. Indeed, the relative residual error (RRE) of EPILE-0 was small. Differences occur for levels that are very small in comparison to the maximum value. PO-MC-H does not perfectly match EPILE-0 because PO does not include all physical phenomena, such as edge diffraction by the C plate. Fig. 5 reveals that PO-AN and PO-MC-H yield similar results, implying that the evanescent waves can be omitted. When surface A was assumed to be infinite, the PO-ANI yielded satisfactory agreement with PO-AN. The advantage of this model is that numerical integration is not required.

In Fig. 4, the vertical lines indicate the specular directions of plate $\text{A}_1 \cup \text{C} \cup \text{A}_2$ (angle θ_0), geometrical paths A_1B_1 (angle θ_1) and B_1A_1 (angle θ_2) defined as

$$\theta_0 = \theta_{\text{inc}}, \theta_{1,2} = -\theta_{\text{inc}} \mp [2(\alpha_B - \alpha_A) + \pi] \text{ modulo } 2\pi. \quad (45)$$

The numerical values are reported in the legend. By plotting the bistatic NRCSs associated with $\psi_{\text{A}_1\text{B}_1}$ and $\psi_{\text{B}_1\text{A}_1}$ (not shown here), we verified that the maxima occurred at $\theta_{1,2}$. Similar results are presented in [22].

Figures 6 and 7 show the monostatic NRCS versus the scattering angle $\theta_{\text{sca}} = -\theta_{\text{inc}}$. The scene is illustrated in Fig. 3. As can be seen, EPILE converges at order 1, and PO-MC-H predicts satisfactory results compared to EPILE-0. For some angles, deviations of PO-MC-H from EPILE-1 occur, suggesting that the triple-bounce contributions are not negligible for these angles. Similar to the bistatic case, the contribution of the evanescent waves can be neglected, and the PO-ANI underestimates the monostatic NRCS when the scattering angle increases. It means that the surface lengths of A_1 and A_2 are not large enough to be considered "infinite".

The results obtained for TE polarization, which are not displayed here, lead to the same conclusions as the TM case in terms of accuracy. PO-MC-H shows results in good agreement with EPILE-2, despite the absence of edge diffraction. The evanescent waves can be neglected, and the additional assumption of PO-ANI gives satisfactory results. This is valid for both the bistatic and monostatic cases. In the monostatic case, some angles show that the triple reflections and the finite lengths of the sea surface cannot be neglected anymore.

4.3. Rough Sea Surface: Coherent Component

In this subsection, we focus on the coherent NRCS when the sea surface is rough. The sea surface obeys a Gaussian process with a zero-height mean value and height variance σ_ξ^2. The sea spectrum was obtained using the Elfouhaily et al. model [20]. First, a wind speed $u_{10} = 3\,\text{m/s}$ defined at ten meters above sea level is considered, giving $\sigma_\xi \approx 0.0572\,\text{m}$. The coherent normalized radar cross section is defined as

$$\text{NRCS}_{\text{Coh}} = \lim_{r' \to \infty} \frac{r'}{2\eta_0} \frac{|\langle \psi \rangle|^2}{p_{\text{inc}}}, \quad (46)$$

where $\langle \cdot \rangle$ denotes the ensemble average operator estimated using a Monte Carlo process by generating n_r independent realizations $\xi_{i \in [1;n_r]}$ of the sea surface. For each surface i, the scattered field ψ_i is computed from either PO or EPILE, and the average operator $\langle \cdot \rangle$ is defined as

$$\langle \psi_i \rangle = \frac{1}{n_r} \sum_{i=1}^{i=n_r} \psi_i. \quad (47)$$

Figure 8 plots the coherent bistatic NRCS in dB scale versus the scattering angle θ_{sca} for $\theta_{\text{inc}} = 30°$. The scene is shown in Fig. 3, but $u_{10} = 3\,\text{m/s}$ and $n_r = 100$. As we can see, only the C plate contributes to the NRCS because "PO-MC-H: Total" well matches with "PO-MC-H: C". It means that the coherent intensities coming from the double reflections and the sea surface do not contribute. Indeed, in the specular direction $\theta_{\text{sca}} = \theta_{\text{inc}}$ and in Eqs. (37), (A8), (A12), the Rayleigh roughness parameter $k_0 \sigma_z \cos\theta_{\text{inc}} \approx 3.11$ ($\sigma_z \approx 0.0572\,\text{m}$ and $k_0 = 2\pi f / c_0 \approx 62.83\,\text{rad/m}$, with $c_0 \approx 3 \times 10^8\,\text{m/s}$). The term $\exp(-4[k_0 \sigma_z \cos\theta_{\text{inc}}]^2) \approx 1.5 \times 10^{-17}$. Fig. 8 also shows a

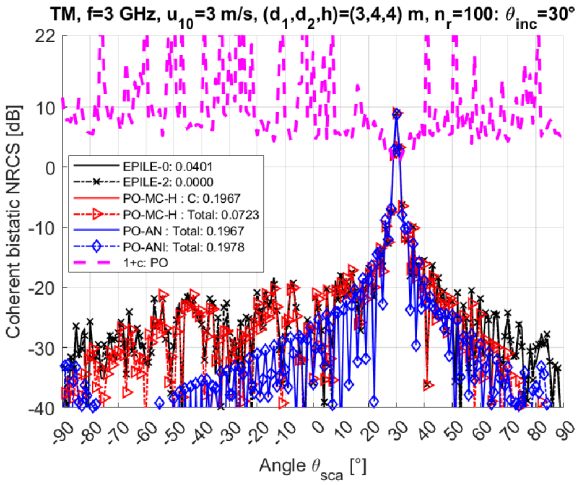

FIGURE 8. Bistatic coherent NRCS in dB scale versus the scattering angle θ_{sca} for $\theta_{\text{inc}} = 30°$. The scene is shown in Fig. 3, but the sea surface is rough with $u_{10} = 3$ m/s and $n_r = 100$.

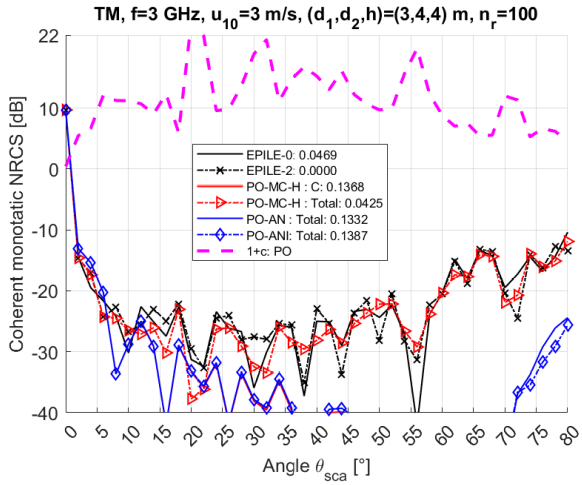

FIGURE 9. Monostatic coherent NRCS in dB scale versus the scattering angle $\theta_{\text{sca}} = -\theta_{\text{inc}}$. The scene is shown in Fig. 3, but the sea surface is rough with $u_{10} = 3$ m/s and $n_r = 100$.

good agreement between PO-MC-H and EPILE-0, and the difference between EPILE-0 and EPILE-2 is weak.

As described in [23], the coherent NRCS estimated from a Monte Carlo process, $\text{NRCS}_{\text{Coh,MC}}$, is related to the theoretical one, NRCS_{Coh}, by

$$\text{NRCS}_{\text{Coh,MC}} = (1 + c)\,\text{NRCS}_{\text{Coh}}, \tag{48}$$

where

$$c = \sqrt{\frac{2}{n_r \beta}}\sqrt{1 + \frac{1}{2\beta(n_r - 1)}}, \tag{49}$$

where n_r is the number of surface realizations, and $\beta = \text{NRCS}_{\text{Coh}}/\text{NRCS}_{\text{Inc}}$ represents the ratio of the coherent to incoherent NRCS (defined later by Eq. (50)). The relative precision of the ensemble average estimation is, therefore, determined by $n_r\beta$, so that only a small number of realizations is required for cases with high coherence (slightly rough surface, i.e., $k_0\sigma_\xi \cos\theta_{\text{inc}} \ll 1$ and $c \to 0$), but a much larger number of realizations is needed to estimate a small coherent field in the presence of a stronger incoherent field (very rough surface, i.e., $k_0\sigma_\xi \cos\theta_{\text{inc}} \gg 1$ and $c \gg 1$).

At microwave frequencies, the sea surface is very rough because $k_0\sigma_z \approx 3.6$ for $f = 3$ GHz. In Fig. 8, $1 + c$ is plotted in dB scale. As expected, near the specular direction, PO-MC-H and PO-AN match well because $1 + c \approx 0$ dB, whereas away from this direction, more surface realizations are needed to converge to the theoretical value given by PO-AN. For $n_r = 300$, simulations not depicted here show that the agreement between PO-MC-H and PO-AN was better.

Figure 9 plots the monostatic coherent NRCS in dB scale versus the scattering angle $\theta_{\text{sca}} = -\theta_{\text{inc}}$. As the scattering angle θ_{sca} grows, the monotastic NRCS drastically decreases, and like the bistatic case, only plate C contributes. Near $\theta_{\text{sca}} = 0$, PO-AN, PO-ANI, PO-MC-H, and EPILE-2 match well, and as θ_{sca} increases, PO-MC-H and PO-AN differ, whereas PO-MC-H and EPILE-2 predict similar results. Like for the bistatic case, more realizations are needed for the PO-MC-H converging toward PO-AN. For θ_{sca} near 80 degrees, the NRCS increases due to the contribution of the double bounce given by ψ_{AB} and ψ_{BA}. For $\theta_{\text{sca}} = 80°$, the Rayleigh roughness parameter $k_0\sigma_z \cos\theta_{\text{inc}} \approx 0.62$ and $\exp(-4[k_0\sigma_z \cos\theta_{\text{inc}}]^2) \approx 0.21$, which explains why the NRCS goes up. In addition, PO-ANI matches well with PO-AN. For $n_r = 300$, the results not reported here clearly show that PO-MC-H converges toward PO-AN over a broader angular range of θ_{sca}.

The results obtained for the TE polarization (not displayed here) lead to the same conclusions in terms of the accuracy of PO-MC-H, PO-AN, and PO-ANI in comparison to EPILE-2. We observe that PO-AN and PO-ANI give similar results, and PO-MC-H nearly coincides with EPILE-2.

For $u_{10} = 6$ m/s, the height standard deviation $\sigma_\xi \approx 0.23$ m and for $\theta_{\text{inc}} = 80°$, the Rayleigh roughness parameter $k_0\sigma_z \cos\theta_{\text{inc}} \approx 2.51$, and the term $\exp(-4[k_0\sigma_z \cos\theta_{\text{inc}}]^2) \approx 1.04 \times 10^{-11}$. For the TM polarization and for $u_{10} = 6$ m/s, unlike in Fig. 9, near grazing angles, the monostatic coherent NRCS vanishes (not shown here).

4.4. Rough Sea Surface: Incoherent Component

The incoherent NRCS is defined as

$$\begin{aligned}\text{NRCS}_{\text{Inc}} &= \lim_{r'\to\infty} \frac{r'}{2\eta_0} \frac{\left\langle |\psi|^2 \right\rangle - |\langle\psi\rangle|^2}{p_{\text{inc}}} \\ &= \lim_{r'\to\infty} \frac{r'}{2\eta_0} \frac{\left\langle |\psi - \langle\psi\rangle|^2 \right\rangle}{p_{\text{inc}}}.\end{aligned} \tag{50}$$

To quantify the incoherence among the four contributions ψ_i, where $i = \{\text{A}, \text{B}, \text{AB}, \text{BA}\}$, an incoherent NRCS square matrix of size 4 is introduced. An element, $\text{NRCS}_{\text{Inc},i,j}$, is defined as follows:

$$\text{NRCS}_{\text{Inc},i,j} = \lim_{r'\to\infty} \frac{r'}{2\eta_0} \frac{\left\langle \psi_i \psi_j^* \right\rangle - \left\langle \psi_i \right\rangle \left\langle \psi_j^* \right\rangle}{p_{\text{inc}}}, \tag{51}$$

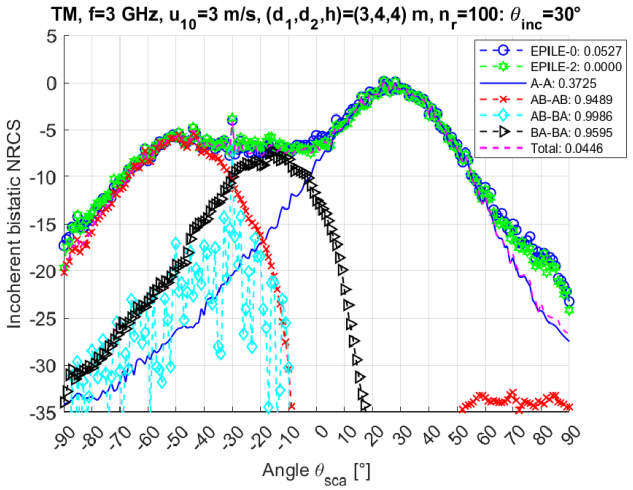

FIGURE 10. Bistatic incoherent NRCS in dB scale versus the scattering angle θ_{sca} for $\theta_{\text{inc}} = 30°$. The scene is shown in Fig. 3, but the sea surface is rough with $u_{10} = 3\,\text{m/s}$ and $n_r = 100$.

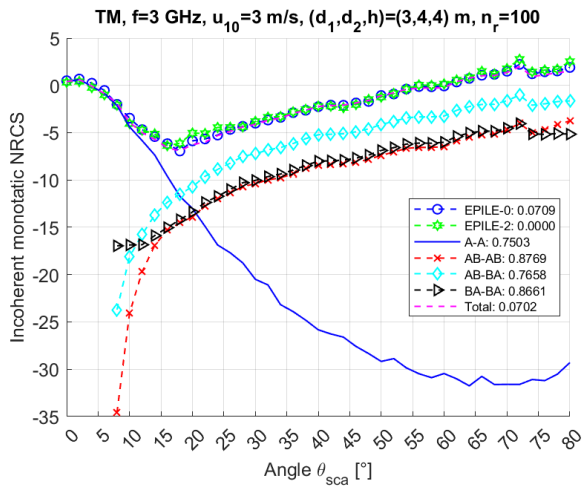

FIGURE 11. Monostatic incoherent NRCS in dB scale versus the scattering angle $\theta_{\text{sca}} = -\theta_{\text{inc}}$. The scene is shown in Fig. 3, but the sea surface is rough with $u_{10} = 3\,\text{m/s}$ and $n_r = 100$.

where the symbol * represents the complex conjugate operator and $j = \{\text{A}, \text{B}, \text{AB}, \text{BA}\}$. Since $\langle \psi_i \psi_j^* \rangle = \langle \psi_j^* \psi_i \rangle^*$, the matrix is Hermitian and

$$\text{NRCS}_{\text{Inc},i,j} + \text{NRCS}_{\text{Inc},j,i} = 2\text{Re}\left(\text{NRCS}_{\text{Inc},i,j}\right), \; i > j, \quad (52)$$

where Re denotes the real part. In conclusion, only $(16-4)/2+4 = 10$ elements are computed, corresponding to the centered inter-correlation $\text{NRCS}_{\text{Inc},i,j}$ between the scattered fields ψ_i and ψ_j^* for $i > j$. For $i = j$, the incoherent NRCS (50) is retrieved, corresponding to the centered auto-correlation of the scattered field ψ_i. In addition,

$$\text{NRCS}_{\text{Inc},i,j} \rightarrow \begin{cases} \text{NRCS}_{\text{Inc},i,i}, & i = j \\ \text{Eq. (52)}, & \text{otherwise} \end{cases}. \quad (53)$$

In this section, from a Monte Carlo process, the 10 incoherent NRCSs $\{\text{NRCS}_{\text{Inc},i,j}\}$ are evaluated from the PO and compared with MoM-EPILE. The estimator is evaluated using Eq. (47). This study will allow us to quantify the factors that contribute the most, with the aim being able to calculate them using a full-analytical derivation, similar to the coherent components.

Figure 10 plots the bistatic incoherent NRCS in dB scale versus the scattering angle θ_{sca} for $\theta_{\text{inc}} = 30°$. The scene is shown in Fig. 3, but the sea surface is rough with $u_{10} = 3\,\text{m/s}$ and $n_r = 100$. Fig. 11 plots the monostatic one. For instance, in the legend, A-A corresponds to $\text{NRCS}_{\text{Inc,A,A}}$. For all the simulations, the contributions for which $i = \{\text{A}, \text{B}\}$ and $j = \{\text{A}, \text{B}, \text{AB}, \text{BA}\}$, except $\text{NRCS}_{\text{Inc,A,A}}$, are not plotted because they are negligible. In other words, only the four NRCSs, $\text{NRCS}_{\text{Inc,A,A}}$, $\text{NRCS}_{\text{Inc,AB,AB}}$, $\text{NRCS}_{\text{Inc,AB,BA}}$, and $\text{NRCS}_{\text{Inc,BA,BA}}$ give noticeable strengths. Numerically, the sum of the four previous incoherent NRCSs equals the total one, named "Total" in the following part.

For the bistatic case, as shown in Fig. 10, EPILE-0 gives the main contribution, which explains the satisfactory agreement between EPILE-2 and Total (which is computed from PO), except for $\theta_{\text{sca}} > 60°$. In the monostatic case, good agreement is obtained for all $\theta_{\text{sca}} = -\theta_{\text{inc}}$. Near the specular direction, Fig. 10 shows that only the sea surface contributes, whereas for $\theta_{\text{sca}} \in [-90; 0]°$, the double-bounce contributions must be accounted for. In the monostatic case, when the strength of $\text{NRCS}_{\text{Inc,A,A}}$ becomes negligible (for $\theta_{\text{sca}} > 20°$), the three other incoherent NRCSs predominate and $\text{NRCS}_{\text{Inc,AB,AB}} \approx \text{NRCS}_{\text{Inc,BA,BA}}$. For the component $\text{NRCS}_{\text{Inc,AB,BA}}$, Fig. 10 also reveals a well-known phenomenon [24–28] called "backscattering enhancement". This occurs for scattering from a single rough surface with high slopes, for which the double-bounce phenomenon contributes.

Indeed, $\text{NRCS}_{\text{Inc,AB,BA}}$ predicts a peak centered around $\theta_{\text{sca}} = -\theta_{\text{inc}}$ with a small width. This component is calculated from $\langle \psi_{\text{AB}} \psi_{\text{BA}}^* \rangle$ and is maximum when $\psi_{\text{BA}} = \psi_{\text{AB}}^*$, giving $\left\langle |\psi_{\text{AB}}|^2 \right\rangle$. In other words, the correlation between ψ_{AB} and ψ_{BA}^* is the maximum. This condition is fully satisfied in the backscattering direction.

These simulations clearly show the relevance of deriving an analytical model, such as the PO. Its main advantage, in comparison to a full-wave method, such as the MoM, is its ability to isolate the different contributions and help better understand the physical phenomena involved in the scattering process.

Figure 12 plots the same variations as in Fig. 10, but for a higher wind speed $u_{10} = 6\,\text{m/s}$. In comparison to Fig. 10, the difference between EPILE-2 and Total is weak, except for $\theta_{\text{sca}} > 70°$. In addition, as expected, the width of the lobe around the specular direction is larger for $u_{10} = 6\,\text{m/s}$ because the surface is rougher.

Figure 13 plots the same variations as in Fig. 10, but for a lower frequency $f = 1\,\text{GHz}$ ($u_{10} = 3\,\text{m/s}$). In comparison to Fig. 10, the difference between EPILE-2 and Total is weak, except for $\theta_{\text{sca}} > 60°$, instead of $\theta_{\text{sca}} > 70°$ in Fig. 10. As the frequency decreased, the edge diffraction by the top plate increased, which may be the origin of the disagreement. In addition, as expected, the lobe width around the specular direction is smaller for $f = 1\,\text{GHz}$ because the surface is less rough. Fig. 13 also reveals that the peak width around the backscattering direction (related to $\text{NRCS}_{\text{Inc,AB,BA}}$) is larger.

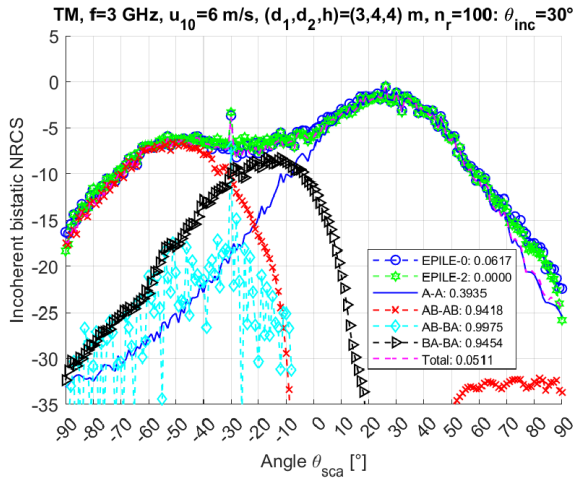

FIGURE 12. Same variations as in Fig. 10, but the wind speed $u_{10} = 6\,\text{m/s}$.

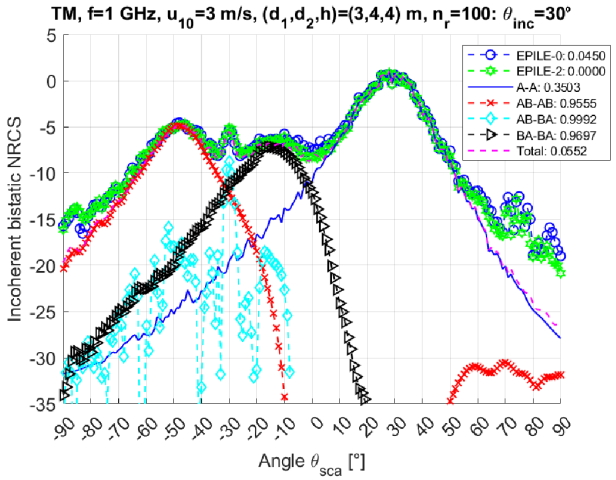

FIGURE 13. Same variations as in Fig. 10, but the frequency is $f = 1\,\text{GHz}$.

For the TE polarization and with the same simulation parameters as in Fig. 10, numerical results not depicted here show that the total NRCS matches well with E-PILE over a larger range of θ_{sca} than that for the TM case, and the levels are similar. In addition, the $\text{NRCS}_{\text{Inc},i,j}$ contributes over the same angular range as for the TM polarization. Moreover, for a monostatic configuration, the numerical results (not displayed here) show a good agreement between Total and EPILE-2.

5. CONCLUSION

In this study, the scattered fields computed from the PO applied at the first and second orders are derived by considering a trapezoidal ship on a rough sea 1D surface. They were compared with the full-wave MoM combined with EPILE, a method distinguishing the contributions versus the number of bounces, like PO.

The results of the coherent NRCS, evaluated from an MC process, show good agreement between PO and MoM-EPILE and also indicate that the evanescent waves may be neglected. In addition, the simulation of the closed-form expression clearly showed that the double reflections contribute less significantly than the single reflections, and the top deterministic plate mainly contributes to the full coherent NRCS. As pointed out in [23], a large number of sea surface realizations is required for the MC results to converge toward the analytical coherent NRCS, because the sea surface is very rough at microwave frequencies.

To quantify the incoherence between the bounces, the centered inter-correlation Hermitian matrix of the scattered fields was also studied using an MC procedure. This is a generalization of the incoherent NRCS definition, and the number of relevant elements equals ten. The numerical results indicated that only four NRCSs contributed to the full incoherent NRCS, that is, the centered auto-correlations $\text{NRCS}_{\text{Inc},i,i}$ with $i = \{\text{A}, \text{AB}, \text{BA}\}$ and $\text{NRCS}_{\text{Inc,AB,BA}}$. In addition, the latter only contributes around the backscattering direction, a phenomenon that is well known for a single rough surface with high slopes and is called "backscattering enhancement". To our knowledge, it is the first time that this phenomenon has been shown for the case of an object on a rough surface. The agreement between PO and MoM-EPILE was good, except for low-grazing scattering angles. This shows that the triple-bounce contributions can be neglected for both the coherent and incoherent NRCSs.

The prospect of this study is to analytically derive the incoherent NRCSs, compare them with MoM-EPILE, and extend the PO derivations to a 3D geometry, which is a difficult task.

APPENDIX A. CASE $L_A \to \infty$

We have

$$\int_{-l^-}^{+l^+} e^{juw} du = \text{Eq. (27)}, \tag{A1}$$

and

$$\int_{-\infty}^{+\infty} e^{juw} du = 2\pi\delta(w), \tag{A2}$$

where δ is the Dirac function. Thus for $l = l^- + l^+$

$$\lim_{l\to\infty} l\,\text{sinc}\left(\frac{lw}{2}\right) = 2\pi\delta(w). \tag{A3}$$

From Eq. (38), if $l_A \to \infty$, then

$$\begin{aligned}\psi_{\text{A},0} &= 2A\,(\boldsymbol{k}_P \cdot \boldsymbol{n}_{A_0})\, e^{j\boldsymbol{r}_{A_0}\cdot\boldsymbol{w}} 2\pi\delta(w) \\ &= 2A\,(\boldsymbol{k}_P \cdot \boldsymbol{n}_{A_0})\, e^{j\boldsymbol{r}_{A_0}\cdot\boldsymbol{w}} 2\pi\delta(w_x + \gamma_{A_0} w_x) \\ &= \mp 4\pi A\delta(\theta_{\text{sca}} - \theta_0),\end{aligned} \tag{A4}$$

where

$$\delta(w(\theta)) = \frac{\delta(\theta)}{|w'(\theta)|}, \tag{A5}$$

where $\mp$ refers to the TE and TM polarizations, respectively. In addition, $\partial w/\partial\theta_{\text{sca}} = k_0\partial(-\sin\theta_{\text{sca}} - \gamma_{A_0}\cos\theta_{\text{sca}})/\partial\theta_{\text{sca}} =$

$k_0(-\cos\theta_{\text{sca}}+\gamma_{A_0}\sin\theta_{\text{sca}})=-\boldsymbol{k}_{\text{sca}}\cdot\boldsymbol{n}_{A_0}$. We also show that $\partial w/\partial\theta_{\text{inc}}=-\boldsymbol{k}_{\text{inc}}\cdot\boldsymbol{n}_{A_0}$, leading to $(\boldsymbol{k}_P\cdot\boldsymbol{n}_{A_0})/|w'(\theta)|=\text{sign}(\boldsymbol{k}_P\cdot\boldsymbol{n}_{A_0})$, where $\theta=\theta_{\text{sca}}$ or $\theta=\theta_{\text{inc}}$ according to the polarization. The slope γ_{A_0} satisfies $w_x+\gamma_{A_0}w_x=0$, yielding $\gamma_{A_0}=-w_x/w_z=\tan([\theta_{\text{inc}}-\theta_{\text{sca}}]/2)$ or $\theta_{\text{sca}}=\theta_{\text{inc}}+2\alpha_A=\theta_0$, where $\gamma_{A_0}=\tan\alpha_A$. Thus, we showed that $\text{sign}(\boldsymbol{k}_P\cdot\boldsymbol{n}_{A_0})=\mp1$ for the TE and TM polarizations, respectively. As expected, this is equal to the Fresnel reflection coefficient of a perfectly-conducting surface.

As $l_A\to\infty$, for the component $\langle\psi_{\text{AB}}\rangle$, from Eq. (41), we have

$$F\left(k_{1,x}+\gamma_{A_0}k_{1,z},l_A^+,l_A^-\right)=2\pi\delta\left(k_{1,x}+\gamma_{A_0}k_{1,z}\right),\quad\text{(A6)}$$

where $k_{1,x}=k_0(\sin\theta_{\text{inc}}-\sin\theta)$ and $k_{1,z}=k_0(-\cos\theta_{\text{inc}}-\cos\theta)$ from Eq. (30) ($\boldsymbol{k_1}=\boldsymbol{k}_{\text{inc}}-\boldsymbol{k}$, $\boldsymbol{k}=k_0(\sin\theta,\cos\theta)$ and $\theta=\pi/2-\alpha$). Using the same method as previously, γ_{A_0} satisfies $k_{1,x}+\gamma_{A_0}k_{1,z}=0$ if

$$\theta=\theta_{\text{inc}}-2\alpha_A=\theta_0.\quad\text{(A7)}$$

Moreover, we show that $(\boldsymbol{k}_A\cdot\boldsymbol{n}_{A_0})/|w'(\theta)|=\mp1$ for the TE and TM polarizations. From Eq. (30), this implies that $\boldsymbol{k}=(\sin\theta_0,\cos\theta_0)=\boldsymbol{k}_0$, $\boldsymbol{k}_1=\boldsymbol{k}_{\text{inc}}-\boldsymbol{k}=\boldsymbol{k}_{\text{inc}}-\boldsymbol{k}_0=\boldsymbol{k}_{10}$, $\boldsymbol{k}_2=\boldsymbol{k}-\boldsymbol{k}_{\text{sca}}=\boldsymbol{k}_0-\boldsymbol{k}_{\text{sca}}=\boldsymbol{k}_{20}$, and Eq. (41) is simplified as follows:

$$\langle\psi_{\text{AB}}\rangle=\mp2A\left(\boldsymbol{k}_{B0}\cdot\boldsymbol{n}_B\right)F\left(k_{20,x}+\gamma_{B_0}k_{20,z},l_B^+,l_B^-\right)$$

$$\times e^{j\boldsymbol{r}_{A_0}\cdot\boldsymbol{k}_{10}+j\boldsymbol{r}_{B_0}\cdot\boldsymbol{k}_{20}}e^{-k_{10,z}^2\sigma_\xi^2/2},\quad\text{(A8)}$$

and

$$\text{TE: }\boldsymbol{k}_{B0}=\boldsymbol{k}_0;\quad\text{TM: }\boldsymbol{k}_{B0}=\boldsymbol{k}_{\text{sca}}.\quad\text{(A9)}$$

If $\alpha_A=0$ (horizontal plate), then $\theta_0=\theta_{\text{inc}}$, $\boldsymbol{k}_0=k_0(\sin\theta_{\text{inc}},\cos\theta_{\text{inc}})$ and $\boldsymbol{k}_{10}=-2k_0\cos\theta_{\text{inc}}\hat{\boldsymbol{z}}$. The modulus of F is maximum if $k_{20,x}+\gamma_{B_0}k_{20,z}=0$, leading to

$$\theta_0=\pi-2\alpha_B-\theta_{\text{sca}}.\quad\text{(A10)}$$

Equaling Eqs. (A7) and (A10), yielding $\theta_{\text{sca}}=\pi-\theta_{\text{inc}}-2(\alpha_B-\alpha_A)$, which corresponds to the specular direction (under the geometrical optics approximation) given by Eq. (45).

For the component $\langle\psi_{\text{BA}}\rangle$, the following Dirac delta function $\delta\left(K_{1,x}+\gamma_{A_0}K_{1,z}\right)$ occurs, where $K_{1,x}=-\sin\theta_{\text{sca}}-\sin\theta$ and $K_{1,z}=-\cos\theta_{\text{sca}}-\cos\theta$. Using the same method as previously, $K_{1,x}+\gamma_{A_0}K_{1,z}=0$ if

$$\theta=-\theta_{\text{sca}}-2\alpha_A=\theta_0.\quad\text{(A11)}$$

We show that $(\boldsymbol{K}_A\cdot\boldsymbol{n}_{A_0})/|w'(\theta)|=\mp1$ for the TE and TM polarization, respectively. From Eq. (32), this implies that $\boldsymbol{k}=(\cos\theta_0,\sin\theta_0)=\boldsymbol{k}_0$, $\boldsymbol{K}_1=-\boldsymbol{k}_{\text{sca}}-\boldsymbol{k}=-\boldsymbol{k}_{\text{sca}}-\boldsymbol{k}_0=\boldsymbol{K}_{10}$, $\boldsymbol{K}_2=\boldsymbol{k}+\boldsymbol{k}_{\text{inc}}=\boldsymbol{k}_0+\boldsymbol{k}_{\text{inc}}=\boldsymbol{K}_{20}$ and Eq. (42) is simplified as follows:

$$\langle\psi_{\text{BA}}\rangle=\mp2A\left(\boldsymbol{K}_{B0}\cdot\boldsymbol{n}_B\right)F\left(K_{20,x}+\gamma_{B_0}K_{20,z},l_B^+,l_B^-\right)$$

$$\times e^{j\boldsymbol{r}_{A_0}\cdot\boldsymbol{K}_{10}+j\boldsymbol{r}_{B_0}\cdot\boldsymbol{K}_{20}}e^{-K_{20,z}^2\sigma_\xi^2/2},\quad\text{(A12)}$$

where

$$\text{TE: }\boldsymbol{K}_{B0}=\boldsymbol{k}_{\text{inc}};\quad\text{TM: }\boldsymbol{K}_{B0}=-\boldsymbol{k}_0.\quad\text{(A13)}$$

If $\alpha_A=0$ (horizontal plate), then $\theta_0=-\theta_{\text{sca}}$, $\boldsymbol{k_0}=k_0(-\sin\theta_{\text{sca}},\cos\theta_{\text{sca}})$ and $\boldsymbol{K}_{10}=-2k_0\cos\theta_{\text{sca}}\hat{\boldsymbol{z}}$. The modulus of F is maximum if $K_{20,x}+\gamma_{B_0}K_{20,z}=0$, leading to

$$\theta_0=\pi-2\alpha_B+\theta_{\text{inc}}.\quad\text{(A14)}$$

Equaling Eqs. (A11) and (A14), this yields $\theta_{\text{sca}}=-\pi-\theta_{\text{inc}}+2(\alpha_B-\alpha_A)$, which corresponds to the specular direction (under the geometrical optics approximation) given by Eq. (45).

APPENDIX B. CASE OF A THORSOS WAVE

Function F assumes that the incident wave is plane, that is $\psi_{\text{inc}}=e^{jk_0(x\sin\theta_{\text{inc}}-z\cos\theta_{\text{inc}})}$. For a Thorsos wave, this function is weighted by a Gaussian tapered wave, and a phase correction is added to better verify the Helmholtz propagation equation. With $u=x-x_{i_0}$, the function F defined by (27) becomes (from Eq. (32) of [5])

$$F\approx\int_{-l^-}^{+l^+}e^{jwu}e^{-\frac{[u+x_{i_0}+(z_{i_0}+\gamma_{i_0}u)\tan\theta_{\text{inc}}]^2}{g^2}}du,\quad\text{(B1)}$$

where (x_{i_0},z_{i_0}) are the coordinates of the plate center. Collecting the terms over u and using the following identity [29]

$$\int e^{-au^2-2bu}du=\frac{1}{2}\sqrt{\frac{\pi}{a}}e^{\frac{b^2}{a}}\text{erf}\left(\sqrt{a}u+\frac{b}{\sqrt{a}}\right),\quad\text{(B2)}$$

where erf is the error function, the integration over $u\in[u^-;u^+]$ leads to

$$F=\frac{1}{2}\sqrt{\frac{\pi}{a}}e^{-\frac{\alpha^2}{g^2}}\left[\text{erfc}\left(u^-\right)-\text{erfc}\left(u^+\right)\right],\quad\text{(B3)}$$

where

$$\alpha=x_{i_0}+z_{i_0}\tan\theta_{\text{inc}},\beta=1+\gamma_{i_0}\tan\theta_{\text{inc}},\quad\text{(B4)}$$

$$a=\frac{\beta^2}{g^2},b=-\frac{jw}{2}+\frac{\alpha\beta}{g^2},u^\pm=\pm\sqrt{a}l^\pm+\frac{b}{\sqrt{a}},\quad\text{(B5)}$$

where $\text{erfc}(x)=1-\text{erf}(x)$ is the complementary error function. For $|u^\pm|\gg1$, a numerical problem arises. To alleviate this, the following expansion is applied [29]

$$\sqrt{\pi}e^{u^2}\text{erfc}(u)\approx\frac{1}{u},\quad\text{(B6)}$$

leading to

$$\frac{1}{2}\sqrt{\frac{\pi}{a}}\text{erfc}\left(u\right)\approx\frac{e^{-al^2-2bl}}{2(al+b)}\approx\frac{e^{-2bl}}{2b}\approx-\frac{e^{jwl}}{jw}.\quad\text{(B7)}$$

Since $a\to0$ ($g\to\infty$ to reach a plane wave), $b\to-jw/2$. The above equation is a primitive of $-e^{jwu}$ evaluated at $u=l^\mp$, which is consistent with Eq. (B1) for $g\to\infty$.

REFERENCES

[1] Johnson, J. T., "A study of the four-path model for scattering from an object above a half space," *Microwave and Optical Technology Letters*, Vol. 30, No. 2, 130–134, 2001.

[2] Johnson, J. T., "A numerical study of scattering from an object above a rough surface," *IEEE Transactions on Antennas and Propagation*, Vol. 50, No. 10, 1361–1367, 2002.

[3] Wei, Y., L. Guo, and S. Chai, "The simulation of EM scattering from target above sea surface with a new four-path model," in *2019 IEEE International Conference on Computational Electromagnetics (ICCEM)*, 1–3, Shanghai, China, 2019.

[4] Harrington, R. F., *Field Computation by Moment Methods*, Macmillan, New York, 1968.

[5] Bourlier, C., N. Pinel, and G. Kubické, *Method of Moments for 2D Scattering Problems: Basic Concepts and Applications*, John Wiley & Sons, London, UK, 2013.

[6] Tsang, L., J. A. Kong, K.-H. Ding, and C. O. Ao, *Scattering of Electromagnetic Waves: Numerical Simulations*, John Wiley & Sons, New York, 2000.

[7] Kubické, G., C. Bourlier, and J. Saillard, "Scattering by an object above a randomly rough surface from a fast numerical method: Extended PILE method combined with FB-SA," *Waves in Random and Complex Media*, Vol. 18, No. 3, 495–519, 2008.

[8] Kubické, G., C. Bourlier, and J. Saillard, "High-frequency bistatic scattering by depolarizing, nearly omnidirectional reflectors: Higher order polyhedral reflectors," *IEEE Transactions on Antennas and Propagation*, Vol. 56, No. 9, 3029–3035, 2008.

[9] Voronovich, A., "Small-slope approximation for electromagnetic wave scattering at a rough interface of two dielectric halfspaces," *Waves in Random Media*, Vol. 4, No. 3, 337, 1994.

[10] Gedney, J. J., J. T. Johnson, and R. J. Burkholder, "An analytical formulation for the coherent scattered field of a target above a randomly rough surface," *IEEE Transactions on Antennas and Propagation*, Vol. 73, No. 1, 329–340, 2025.

[11] Voronovich, A. G., *Wave Scattering from Rough Surfaces*, Springer, 1999.

[12] Di Simone, A., W. Fuscaldo, L. M. Millefiori, D. Riccio, G. Ruello, P. Braca, and P. Willett, "Analytical models for the electromagnetic scattering from isolated targets in bistatic configuration: Geometrical optics solution," *IEEE Transactions on Geoscience and Remote Sensing*, Vol. 58, No. 2, 861–880, 2020.

[13] Zhang, Y., Y. E. Yang, H. Braunisch, and J. A. Kong, "Electromagnetic wave interaction of conducting object with rough surface by hybrid SPM/MOM technique," *Progress In Electromagnetics Research*, Vol. 22, 315–335, 1999.

[14] Ye, H. and Y.-Q. Jin, "A hybrid analytic-numerical algorithm of scattering from an object above a rough surface," *IEEE Transactions on Geoscience and Remote Sensing*, Vol. 45, No. 5, 1174–1180, 2007.

[15] Guan, B., J. F. Zhang, X. Y. Zhou, and T. J. Cui, "Electromagnetic scattering from objects above a rough surface using the method of moments with half-space Green's function," *IEEE Transactions on Geoscience and Remote Sensing*, Vol. 47, No. 10, 3399–3405, 2009.

[16] Man, M., Z. Lei, Y. Xie, and X. Li, "Bistatic RCS prediction of composite scattering from electrically very large ship-sea geometry with a hybrid facet-based KA and shadow-corrected GRECO scheme," *Progress In Electromagnetics Research B*, Vol. 60, 35–48, 2014.

[17] Rashidi-Ranjbar, E. and M. Dehmollaian, "Target above random rough surface scattering using a parallelized IPO accelerated by MLFMM," *IEEE Geoscience and Remote Sensing Letters*, Vol. 12, No. 7, 1481–1485, 2015.

[18] Wei, Y.-W., C.-F. Wang, C. Y. Kee, and T.-T. Chia, "An accurate model for the efficient simulation of electromagnetic scattering from an object above a rough surface with infinite extent," *IEEE Transactions on Antennas and Propagation*, Vol. 69, No. 2, 1040–1051, 2021.

[19] Meng, W., J. Li, Y.-J. Xi, L.-X. Guo, and S.-K. Wen, "Electromagnetic scattering for multiple moving targets above/on a rough surface using multi-dynamic-octrees-based SBR algorithm," *IEEE Transactions on Geoscience and Remote Sensing*, Vol. 61, 1–12, 2023.

[20] Elfouhaily, T., B. Chapron, K. Katsaros, and D. Vandemark, "A unified directional spectrum for long and short wind-driven waves," *Journal of Geophysical Research*, Vol. 102, No. C7, 781–796, 1997.

[21] Thorsos, E. I., "The validity of the Kirchhoff approximation for rough surface scattering using a Gaussian roughness spectrum," *The Journal of the Acoustical Society of America*, Vol. 83, No. 1, 78–92, 1988.

[22] Jin, Y.-Q. and Z. Li, "Numerical simulation of radar surveillance for the ship target and oceanic clutters in two-dimensional model," *Radio Science*, Vol. 38, No. 3, 11–1–11–6, 2003.

[23] Raines, E., J. T. Johnson, and R. J. Burkholder, "Characterizing the coherent reflected power dependence on rough surface height at low signal levels," in *IGARSS 2020 — 2020 IEEE International Geoscience and Remote Sensing Symposium*, 3444–3446, Waikoloa, HI, USA, 2020.

[24] Kim, M.-J., J. C. Dainty, A. T. Friberg, and A. J. Sant, "Experimental study of enhanced backscattering from one- and two-dimensional random rough surfaces," *Journal of the Optical Society of America A*, Vol. 7, No. 4, 569–577, 1990.

[25] Johnson, J. T., L. Tsang, R. T. Shin, K. Pak, C. H. Chan, A. Ishimaru, and Y. Kuga, "Backscattering enhancement of electromagnetic waves from two-dimensional perfectly conducting random rough surfaces: A comparison of Monte Carlo simulations with experimental data," *IEEE Transactions on Antennas and Propagation*, Vol. 44, No. 5, 748, 1996.

[26] Ishimaru, A., C. Le, Y. Kuga, L. Ailes-Sengers, and T. K. Chan, "Polarimetric scattering theory for high slope rough surface," *Progress In Electromagnetics Research*, Vol. 14, 1–36, 1996.

[27] Bourlier, C. and G. Berginc, "Multiple scattering in the high-frequency limit with second-order shadowing function from 2D anisotropic rough dielectric surfaces: I. Theoretical study," *Waves in Random Media*, Vol. 14, No. 3, 229, 2004.

[28] Bourlier, C. and G. Berginc, "Multiple scattering in the high-frequency limit with second-order shadowing function from 2D anisotropic rough dielectric surfaces: II. Comparison with numerical results," *Waves in Random Media*, Vol. 14, No. 3, 253, 2004.

[29] Abramowitz, M. and I. A. Stegun, *Handbook of Mathematical Functions*, Dover Publications, New York, 1970.